

B-spline Parameterized Joint Optimization of Reconstruction and K-space Trajectories (BJORK) for Accelerated 2D MRI

Guanhua Wang, Tianrui Luo, Jon-Fredrik Nielsen, Douglas C. Noll, and Jeffrey A. Fessler

Abstract—Optimizing k-space sampling trajectories is a challenging topic for fast magnetic resonance imaging (MRI). This work proposes to optimize a reconstruction algorithm and sampling trajectories jointly concerning image reconstruction quality. We parameterize trajectories with quadratic B-spline kernels to reduce the number of parameters and enable multi-scale optimization, which may help to avoid sub-optimal local minima. The algorithm includes an efficient non-Cartesian unrolled neural network-based reconstruction and an accurate approximation for back-propagation through the non-uniform fast Fourier transform (NUFFT) operator to accurately reconstruct and back-propagate multi-coil non-Cartesian data. Penalties on slew rate and gradient amplitude enforce hardware constraints. Sampling and reconstruction are trained jointly using large public datasets. To correct the potential eddy-current effect introduced by the curved trajectory, we use a pencil-beam trajectory mapping technique. In both simulations and in-vivo experiments, the learned trajectory demonstrates significantly improved image quality compared to previous model-based and learning-based trajectory optimization methods for 20× acceleration factors. Though trained with neural network-based reconstruction, the proposed trajectory also leads to improved image quality with compressed sensing-based reconstruction.

Index Terms—Magnetic resonance imaging, non-Cartesian sampling, deep learning, eddy-current effect, image reconstruction

I. INTRODUCTION

Magnetic Resonance Imaging (MRI) systems acquire raw data in the frequency domain (k-space). Most scanning protocols sample data points sequentially according to a pre-determined sampling pattern. The most common sampling patterns are variants of Cartesian rasters and non-Cartesian trajectories such as radial spokes [1] and spiral interleaves [2]. The local smoothness of these patterns facilitates to ensure that they obey hardware limits, namely the maximum gradient and slew rate that constrain the speed and acceleration when traversing k-space. These patterns also make it easy to ensure sufficient sampling densities. In recent years, hardware improvements, especially with the RF and gradient systems,

enable more complex gradient waveform designs and sampling patterns. For a given readout time, optimized designs can cover a broader and potentially more useful region in k-space, reducing the overall scanning time and/or improving image quality, particularly when combined with multiple receive coils.

For fast imaging, many works focus on acceleration in the phase-encoding (PE) direction with fully sampled frequency-encoding (FE) lines [3]–[7]. Usually, there is enough time for the Δk shift in the PE direction, so gradient and slew rate constraints are readily satisfied. More general non-Cartesian trajectory designs in 2D and 3D can further exploit the flexibility in the FE direction. However, in addition to hardware physical constraints, the system is affected by imperfections such as the eddy currents that cause the actual trajectory to deviate from the nominal one and introduce undesired phase fluctuations in the acquired data [8]. Some studies optimize properties of existing trajectories such as the density of spiral trajectories [9] or the rotation angle of radial trajectories [10]. More complex waveforms, e.g., wave-like patterns [11], can provide more uniform coverage of k-space and mitigate aliasing artifacts. To accommodate the incoherence requirements of compressed sensing based methods, [12], [13] introduce slight perturbations to existing trajectories, like radial or spiral trajectories. Some works also explore genetic algorithms to solve this non-convex constrained problem [14].

The recent SPARKLING method [15] considers two criteria for trajectory design: (1) the trajectory should match a pre-determined density according to a certain measure, and (2) the sampling points should be locally uniform to avoid clusters or gaps. The density and uniformity criteria are transformed into “attraction” and “repulsion” forces among the sampling points. The work uses fast multipole methods (FMM) [16] to efficiently calculate the interactions between points. Projection-based optimization handles the gradient and slew rate constraints [17]. In-vivo and simulation experiments demonstrate that this approach reduces the level of aliasing artifacts for 2D and 3D T2*-weighted imaging. However, in SPARKLING, the density is determined heuristically; determining the optimal sampling density for different protocols remains an open problem. The work also does not consider some k-space signal characteristics such as conjugate symmetry. Furthermore, the point spread function (PSF) of the calculated trajectory for high under-sampling rates is not guaranteed to be optimal for reconstruction algorithms like those based on convolution

This work is supported in part by NIH Grants R01 EB023618 and U01 EB026977, and NSF Grant IIS 1838179.

G. Wang, T. Luo, J.-F. Nielsen, and D. C. Noll are with the Department of Biomedical Engineering, University of Michigan, Ann Arbor, MI 48109 USA (e-mails: {guanhuaw, tianrui, jfn, dnoll}@umich.edu).

J. A. Fessler is with the Department of EECS, University of Michigan, Ann Arbor, MI 48109 USA (e-mail: fessler@umich.edu).

neural networks, because the reconstruction algorithm is not part of the SPARKLING design process.

With rapid advances in deep learning and auto-differentiation software, learning-based signal sampling strategies are being investigated in multiple fields such as optics and ultrasound [18], [19]. In MRI, the majority of learning-based works have focused on sampling patterns of phase encoding locations. Some studies formulate the on-grid sampling pattern as i.i.d samples from multivariate Bernoulli distribution [20], [21]. Since random sampling operations are not differentiable, different surrogate gradients, such as Gumbel-Softmax, are developed in these works. Rather than gradient descent, [22] uses a greedy search method. [23] further reduces the complexity of greedy search by using Pareto optimization, an evolutionary algorithm for sparse regression [24]. Some works have used reinforcement learning. For example, [25] and [26] adopted a double network setting: one for reconstruction and the other generating a sampling pattern, where the first work used Monte-Carlo Tree Search (MCTS) and the second used Q-learning to optimize the 1-D sub-sampling. Instead of using an end-to-end CNN as the reconstruction algorithm in other works, [27] constructs a differentiable compressed sensing reconstruction framework. [28] used an unrolled neural network as the reconstruction algorithm.

To our knowledge, PILOT [29] is the first work to optimize a 2D non-Cartesian trajectory and an image reconstruction method jointly. The training loss is the reconstruction error since the ultimate goal of trajectory optimization is high image quality. The trained parameters were the locations of sampling points and the weights of the reconstruction neural network. Large datasets and stochastic gradient descent were used to optimize the parameters. To meet the hardware limits, a penalty was applied on the gradient and slew rate. Since the reconstruction involves non-Cartesian data, PILOT uses a (bi-linear, hence differentiable) gridding reconstruction algorithm to map the k-space data into the image domain, followed by a U-net [30] to refine the gridded image data. Simulation experiments report encouraging results compared to ordinary trajectories. Nevertheless, the algorithm often gets stuck in sub-optimal local minima where the initial trajectory is only slightly perturbed yet the slew rate rapidly oscillates. To reduce the effect of initialization, the paper uses a randomized initialization algorithm based on the traveling salesman problem (TSP). However, this initialization approach works only with single-shot long TE sequences, limiting its utility in many clinical applications. The implementation in [29] relies on auto-differentiation to calculate the Jacobian of the non-uniform Fourier transform; here we adopt a new NUFFT Jacobian approximation that is faster and more accurate.

To overcome the limitations of previous methods and further expand their possible applications, this paper proposes an improved supervised learning workflow called **B**-spline parameterized **J**oint **O**ptimization of **R**econstruction and **K**-space trajectory (**BJORK**). Our main contributions include the following. (1) We propose to parameterize the trajectories with quadratic B-spline kernels. This reparameterization reduces the number of parameters and enables multilevel optimiza-

tion, enabling non-local improvements to the initial trajectory. Moreover, the local smoothness of B-spline kernels avoids rapid slew rate oscillations. (2) We adopt an unrolled neural network reconstruction method for non-Cartesian sampling patterns. Compared to the end-to-end model implemented in previous works, the proposed approach combines the strength of learning-based and model-based reconstruction, improving the effect of both reconstruction and trajectory learning. (3) We derive a more accurate and efficient approximation of the NUFFT Jacobian matrix. (See Supplementary Materials for derivation and validation.) (4) In addition to a simulation experiment, we also conducted phantom and in-vivo experiments with protocols that differ from the training dataset to evaluate the generalizability and applicability of the model. (5) We used a k-space mapping technique to correct potential eddy current-related artifacts. (6) Compared with SPARKLING, the proposed learning-based approach does not need to assume signal characteristics such as spectrum energy density. Instead, the required sampling trajectories are learned from a large data set in a supervised manner.

The remaining materials are organized as follows. Section II details the proposed method. Section III describes experiment settings and control methods. Sections IV and V present and discuss the results.

II. METHODS

This section describes the proposed approach for supervised learning of the sampling trajectory and image reconstruction method.

A. Problem formulation

Fig. 1 shows the overall workflow of the proposed approach. The goal is to optimize $\omega \in \mathbb{R}^{N_s \times N_d}$, a trainable (possibly multi-shot) sampling pattern, and $\theta \in \mathbb{R}^M$, the M parameters of the image reconstruction method, where N_s denotes the total number of k-space samples, and N_d denotes the image dimensionality. (The results are for $N_d = 2$, i.e., 2D images, but the method is general.)

The training loss for jointly optimizing the parameters is as follows:

$$\begin{aligned} & \arg \min_{\omega \in \mathbb{R}^{N_s \times N_d}, \theta \in \mathbb{R}^M} \mathbb{E}_{\mathbf{x}} \|\mathbf{f}_{\theta}(\omega; \mathbf{A}(\omega)\mathbf{x} + \varepsilon) - \mathbf{x}\| \quad (1) \\ \text{s.t. } & \|\mathbf{D}_1 \omega^{[d]}\|_{\infty} \leq \gamma \Delta t g_{\max}, \\ & \|\mathbf{D}_2 \omega^{[d]}\|_{\infty} \leq \gamma \Delta t^2 s_{\max}, \quad d = 1, \dots, N_d, \end{aligned}$$

where $\mathbf{x} \in \mathbb{C}^{N_v}$ is a fully sampled reference image (batch) having N_v voxels from the training data set and ε is simulated additive complex Gaussian noise. $\mathbf{A} \in \mathbb{C}^{N_s N_c \times N_v}$ denotes the system matrix of MR imaging, where N_c denotes the number of receiver coils. For multi-coil non-Cartesian acquisition, it is a non-Cartesian SENSE operator [31] that applies a pointwise multiplication of the sensitivity maps followed by a NUFFT operator (currently we do not consider field inhomogeneity). $\mathbf{f}_{\theta}(\omega; \cdot)$ denotes an image reconstruction algorithm with parameters θ that is applied to simulated under-sampled data $\mathbf{A}(\omega)\mathbf{x} + \varepsilon$. As detailed in subsection II-C, we use an unrolled

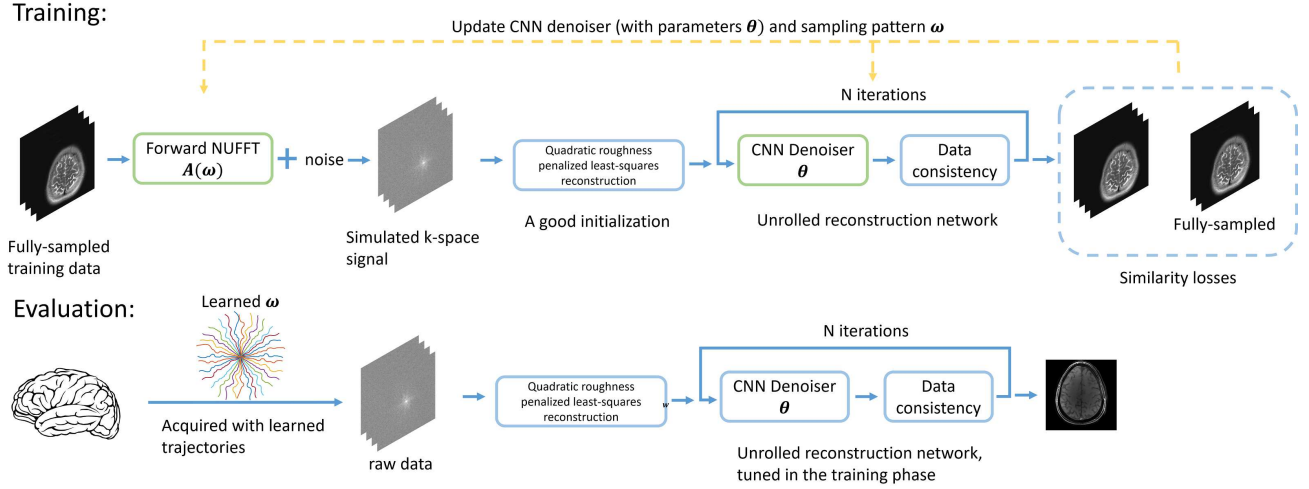


Fig. 1. Diagram for the proposed approach. To optimize the sampling trajectory and the reconstruction algorithm jointly using the stochastic gradient descent (SGD)-type method, we construct a differentiable forward MRI system matrix $\mathbf{A}(\omega)$ that simulates k-space data w.r.t. trajectory ω from ground truth images, and an unrolled neural network that reconstructs the simulated data. The reconstruction errors compared with the ground truth are used as the training loss to update learnable parameters (the trajectory ω and the network's parameters θ).

neural network. The reconstruction loss $\|\cdot\|$ is a combined ℓ_1 and square of ℓ_2 norm. \mathbf{D}_1 and \mathbf{D}_2 are the first-order and second-order finite difference operators. Δt is the dwell time and γ denotes the gyromagnetic ratio. For multi-shot imaging, the difference operator applies to each shot individually. The constraints stand for maximum gradient field strength (g_{\max}) and slew rate (s_{\max}). To use the stochastic gradient descent (SGD) method, we convert the box constraint into a penalty function ϕ , which in our case is a soft-thresholding function, leading to our final optimization problem as follows:

$$\begin{aligned} \arg \min_{\omega \in \mathbb{C}^{N_s \times N_d}, \theta \in \mathbb{R}^M} \mathbb{E}_{\mathbf{x}} \|\mathbf{f}_{\theta, \omega}(\omega; \mathbf{A}(\omega)\mathbf{x} + \varepsilon) - \mathbf{x}\| \quad (2) \\ + \phi_{\gamma \Delta t g_{\max}}(|\mathbf{D}_1 \omega|) \\ + \phi_{\gamma \Delta t^2 s_{\max}}(|\mathbf{D}_2 \omega|). \end{aligned}$$

We update θ and ω simultaneously for each mini-batch of training data.

B. Parameterization and multi-level optimization

We parameterize the sampling pattern with 2nd-order quadratic B-spline kernels:

$$\omega^{[d]} = \mathbf{B}\mathbf{c}^{[d]}, \quad (3)$$

where $\mathbf{B} \in \mathbb{R}^{N_s \times L}$ denotes the interpolation matrix, and $\mathbf{c}^{[d]}$ denotes the d th column of the coefficient matrix $\mathbf{c} \in \mathbb{R}^{L \times N_d}$. L denotes the length of $\mathbf{c}^{[d]}$, or the number of interpolation kernels in each dimension. Using B-spline kernels to parameterize the trajectory reduces the number of individual inequality constraints from $4N_d N_s$ to $4N_d L$ [32], where typically $L \ll N_s$.

As shown in previous works [29], the optimized trajectories are often local minima near the initialization, only slightly perturbing the initial trajectory. We propose to use a multilevel training strategy to improve the optimization process [33]. The decimation rate N_s/L is initialized with a large value (like 64).

Thus, many neighboring sample points are controlled by the same coefficient. After both \mathbf{c} and θ converge, we reduce the decimation rate, typically by a factor of 2, and begin a new round of training initialized with ω and θ of the previous round.

C. Reconstruction

In the joint learning model, we adopted a model-based unrolled neural network (UNN) approach to image reconstruction [34]–[37]. Compared to the previous joint learning model (PILOT) that used a single end-to-end network [29], an unrolled network can lead to a more accurate reconstruction [34].

A typical cost function for regularized MR image reconstruction has the form:

$$\hat{\mathbf{x}} = \arg \min_{\mathbf{x}} \|\mathbf{A}\mathbf{x} - \mathbf{y}\|_2^2 + \mathcal{R}(\mathbf{x}). \quad (4)$$

The first term is usually called the data-consistency term that ensures the reconstructed image is consistent with the acquired k-space data \mathbf{y} . (In the training phase, $\mathbf{A}(\omega)\mathbf{x} + \varepsilon$ is the simulated \mathbf{y} .) The regularization term $\mathcal{R}(\cdot)$ is designed to control aliasing and noise when the data is under-sampled. By introducing an auxiliary variable \mathbf{z} , we replace (4) with the following alternative:

$$\hat{\mathbf{x}} = \arg \min_{\mathbf{x}} \min_{\mathbf{z}} \|\mathbf{A}\mathbf{x} - \mathbf{y}\|_2^2 + \mathcal{R}(\mathbf{z}) + \mu \|\mathbf{x} - \mathbf{z}\|_2^2, \quad (5)$$

where $\mu > 0$ is a penalty parameter. Using an alternating minimization approach, the optimization updates become:

$$\mathbf{x}_{i+1} = \arg \min_{\mathbf{x}} \|\mathbf{A}\mathbf{x} - \mathbf{y}\|_2^2 + \mu \|\mathbf{x} - \mathbf{z}_i\|_2^2, \quad (6)$$

$$\mathbf{z}_{i+1} = \arg \min_{\mathbf{z}} \mathcal{R}(\mathbf{z}) + \mu \|\mathbf{x}_{i+1} - \mathbf{z}\|_2^2. \quad (7)$$

The analytical solution for the \mathbf{x} update is

$$\mathbf{x}_{i+1} = (\mathbf{A}'\mathbf{A} + \mu\mathbf{I})^{-1}(\mathbf{A}'\mathbf{y} + \mu\mathbf{z}_i),$$

but the direct inverse is useful only for single-coil Cartesian sampling. Instead, we use a few iterations of the conjugate gradient (CG) method for the \mathbf{x} update, applying the Toeplitz embedding technique to accelerate computation of $\mathbf{A}'\mathbf{A}$ [38].

For a mathematically defined regularizer, the \mathbf{z} update would be a proximal operator. Here we follow previous work [39] and use a CNN-based denoiser $\mathbf{z}_{i+1} = \mathcal{D}_\theta(\mathbf{x}_{i+1})$. To minimize memory usage and avoid over-fitting, we used the same θ across iterations, though iteration-specific networks may improve the reconstruction result [37].

For the CNN-based denoiser, we used the Deep Iterative Down-Up CNN (DIDN) [40]. As a state-of-art model for image denoising, the DIDN model uses less memory than popular models like U-net [30] with improved reconstruction results. In our experiments, it also led to faster convergence of training than previous denoising networks.

Since neural networks are sensitive to the scale of the input, a good and consistent initial estimate of \mathbf{x} is important. We used the following quadratic roughness penalty approach to compute an initial image estimate:

$$\begin{aligned} \mathbf{x}_0 &= \arg \min_{\mathbf{x}} \|\mathbf{A}\mathbf{x} - \mathbf{y}\|_2^2 + \lambda \|\mathbf{R}\mathbf{x}\|_2^2 \\ &= (\mathbf{A}'\mathbf{A} + \lambda \mathbf{R}'\mathbf{R})^{-1} \mathbf{A}'\mathbf{y}, \end{aligned} \quad (8)$$

where \mathbf{R} denotes the N_d -dimensional first-order finite difference (roughness) operator. We also used the CG method to (approximately) solve this quadratic minimization problem.

D. Correction of eddy-current effect

Rapidly changing gradient waveforms may suffer from eddy-current effects, even with shielded coils. This hardware imperfection requires additional measurements and corrections so that the actual sampling trajectory is used for reconstructing real MRI data. Some previous works used a field probe and corresponding gradient impulse-response (GIRF) model [41]. In this work, we adopted the ‘k-space mapping’ method [8], [42] that does not require additional hardware. Rather than mapping the k_x and k_y separately as in previous papers, we excite a pencil-beam region using one 90° flip and a subsequent 180° spin-echo pulse [43]. We averaged multiple repetitions to estimate the actual acquisition trajectory. We also subtracted a zero-order eddy current phase term from the acquired data [8].

III. EXPERIMENTS

A. Comparison with prior art

We compared the proposed BJORK approach with the SPARKLING method for trajectory design in all experiments¹. The initial trajectories were identical for both BJORK and SPARKLING methods. SPARKLING used the default multi-level optimization strategy and parameter settings, as detailed in [44].

Both BJORK and PILOT [29] are methods for joint sampling design and reconstruction optimization. We compared three key differences between the three methods individually:

(1) the accuracy of the NUFFT Jacobian matrices, as discussed in the Supplementary Materials. (2) the reconstruction method involved. Our BJORK approach uses an unrolled neural network, while PILOT uses a single end-to-end reconstruction neural network in the image domain. (3) the effect of trajectory parameterization².

B. Image quality evaluation

To evaluate the reconstruction quality provided by different trajectories, we used two types of reconstruction methods in the test phase: unrolled neural network (UNN) (with learned θ) and compressed sensing (sparsity regularization for an orthogonal wavelet transform). For SPARKLING and standard undersampled trajectories, the unrolled neural networks θ for reconstruction were trained with the same hyper-parameters as the proposed approach. The only difference is that BJORK learns a trajectory simultaneously whereas SPARKLING uses a trajectory based on a specified sampling density. We also used compressed sensing-based reconstruction to test the generalizability of different kinds of trajectories. The penalty function is the ℓ_1 norm of the orthogonal wavelet transform with a Daubechies 4 wavelet. The ratio between the penalty term and the data-fidelity term is 1e-7. We used the SigPy package³ and its default primal-dual hybrid gradient (PDHG) algorithm. This study used two evaluation metrics: the structural similarity metric (SSIM) and peak signal-to-noise ratio (PSNR) [45].

C. Trajectories

To demonstrate the proposed model’s adaptability, we investigated two types of trajectory initializations: an undersampled in-out radial trajectory with a shorter readout time (≈ 2.5 ms) and an undersampled spiral trajectory with a longer readout time (≈ 16 ms). For the radial initialization, the number of spokes is 16, and each spoke has 640 points of acquisition. The rotation angle is equidistant between $-\pi/2$ and $\pi/2$. For the spiral initialization, the number of shots is 8, and each leaf has around 4000 points. We used the variable-density spiral design package⁴ from [46].

For both simulation and real acquisition, the dwell time for both waveforms and data sampling is set to 4 usec, with a field-of-view (FOV) of 22 cm. The maximum gradient strength is 5 Gauss/cm, and the maximum slew rate is 15 Gauss/cm/ms.

D. Network training and hyper-parameter setting

The simulation experiments used the NYU fastMRI brain dataset to train the trajectories and neural networks [47]. The dataset consists of multiple contrasts, including T1w, T2w, and FLAIR. FastMRI’s knee subset was also used in a separate training run to investigate the influence of training data on learned sampling patterns. The central 320×320 region was cropped to exclude the noise in the air background. Sensitivity maps were estimated using the ESPiRiT method [48] with

²The latest version of PILOT on arXiv [29, version 4] also uses trajectory parameterization and multi-level optimization, focusing on long readout cases.

³<https://github.com/mikgroup/sigpy>

⁴<https://mrsrl.stanford.edu/~brian/vdspiral/>

¹The code will be available on Github if accepted.

TABLE I
PROTOCOLS FOR DATA ACQUISITION

| Protocols for the phantom experiment: | | | | | | | | | |
|---------------------------------------|---------|--------|---------|--------|--------|-----|----------|--------|------|
| Name | FOV(cm) | dz(mm) | Gap(mm) | TR(ms) | TE(ms) | FA | Acqs | dt(us) | Time |
| Radial-like | 22*22*5 | 2 | 0.5 | 13.8 | 2.24 | 15° | 16*640 | 4 | 0:05 |
| Radial-full | 22*22*5 | 2 | 0.5 | 13.8 | 2.24 | 15° | 320*640 | 4 | 1:30 |
| Protocols for the in-vivo experiment: | | | | | | | | | |
| Name | FOV(cm) | dz(mm) | Gap(mm) | TR(ms) | TE(ms) | FA | Acqs | dt(us) | Time |
| Radial-like | 22*22*4 | 2 | 0.5 | 318.4 | 3.56 | 90° | 16*1280 | 4 | 0:05 |
| Radial-full | 22*22*4 | 2 | 0.5 | 318.4 | 3.56 | 90° | 320*1280 | 4 | 1:40 |

dz: slice thickness; Gap: gap between slices; Acqs: number of shots * readout points; FA: flip angle

the central 24 phase-encoding lines, and the corresponding conjugate phase reconstruction was regarded as the ground truth x .

The batchsize was 4. The number of blocks, or the number of outer iterations for the unrolled neural network was 6. The weight μ in (5) could also be learned, but this operation will double the computation load with minor improvement. In the current setting, μ was set to 2. The number of training epochs was set to 10 for each level of B-spline kernel length. We used 4 levels of optimization, and the total number of epochs was 40. For training the network with existing trajectories (radial, spiral, and SPARKLING), we also used 40 training epochs. We used the Adam optimizer [49], with parameter $\beta = [0.5, 0.999]$, for both trajectories ω and network parameters θ . The learning rate linearly decayed from $1e-3$ to 0 for the trajectory update, and from $1e-5$ to 0 for the network update. We did not observe obvious over-fitting phenomena on the validation set.

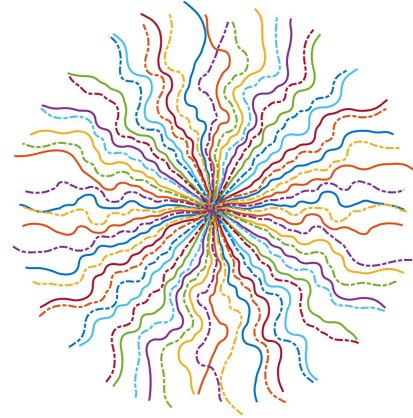


Fig. 3. The dash-dot line shows the 180° rotated BJORK trajectory. The original and rotated trajectory have little overlap, suggesting that the BJORK automatically learned a sampling pattern that exploits k-space symmetry.

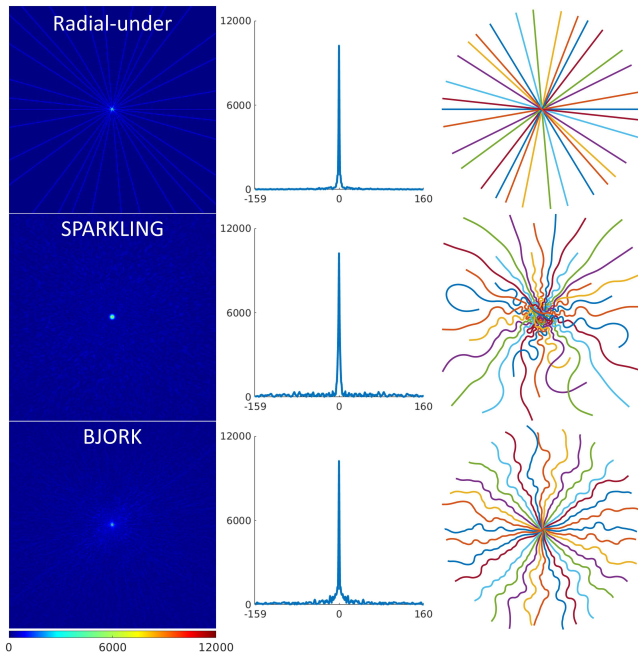


Fig. 2. PSFs of different sampling patterns. The plots show the magnitude of the row across the zero point.

E. Phantom and in-vivo Experiments

Table I details the scanning protocols of the RF-spoiled, gradient echo (GRE) sequences used. For in-vivo acquisitions,

a fat-saturation pulse was applied before the tip-down RF pulse. For radial-like sequences, we tested a GRE sequence with 3 different readout trajectories: standard (golden-angle) undersampled radial, BJORK initialized with undersampled radial, and SPARKLING initialized with undersampled radial. Radial-full means the fully sampled radial trajectory. We also acquired an additional dual-echo Cartesian GRE image, for generating the sensitive map and (potentially) B0 map. The sensitivity maps are generated by ESPIRiT [48] methods. The sequences were programmed with TOPPE [43], and implemented on a GE MR750 3.0T scanner with a Nova Medical 32 channel Rx head coil. For in-vivo imaging, to increase the SNR of acquired signal, the trajectory had a longer readout (≈ 5 ms, 1280 sampling points), trained by the same procedure as in subsection III-D. Subjects gave informed consent under local IRB approval. For phantom experiments, we used a water phantom with 3 internal cylinders.

The k-space mapping was implemented on a water phantom. The thickness of the pencil-beam was $2\text{mm} \times 2\text{mm}$. The trajectory estimates were based on an average of 30 repetitions.

IV. RESULTS

1) *Quantitative results*: The test set includes 950 slices. Table II shows the quantitative results (SSIM and PSNR). The proposed method has significant improvement compared with un-optimized trajectories ($P < 0.005$). It also has improved reconstruction quality compared with SPARKLING when considering unrolled neural network-based reconstruction. For

CS-based reconstruction of radial-like sequences, the results for the SPARKLING trajectory were slightly better than those from the BJORK-optimized trajectory (that was not tuned for CS-based reconstruction). The reason is that CS-based reconstruction using the BJORK trajectory may have some streak artifacts that can be resolved by the neural network-based reconstruction, but that poses a challenge to CS-based reconstruction. Supplementary Materials include several examples of the UNN-based reconstruction of different trajectories. Compared to undersampled radial trajectory or SPARKLING trajectory, the proposed method has a better restoration of details and lower levels of artifacts.

Fig. 2 displays point spread functions of radial-like trajectories. The BJORK PSF has a narrower central-lobe than SPARKLING and much fewer streak artifacts than standard radial. Fig. 3 shows the conjugate symmetry relationship implicitly learned in the BJORK trajectory.

TABLE II

QUANTITATIVE RESULTS FOR SIMULATION EXPERIMENTS

| SSIM: | | | | |
|---------------|-----|----------|--------------|--------------|
| | | Standard | SPARKLING | BJORK |
| radial-like | UNN | 0.958 | 0.963 | 0.968 |
| | CS | 0.911 | 0.927 | 0.921 |
| spiral-like | UNN | 0.985 | 0.978 | 0.989 |
| | CS | 0.958 | 0.924 | 0.961 |
| PSNR (in dB): | | | | |
| | | Standard | SPARKLING | BJORK |
| radial-like | UNN | 35.5 | 36.3 | 37.0 |
| | CS | 33.0 | 34.6 | 33.9 |
| spiral-like | UNN | 43.9 | 38.9 | 44.3 |
| | CS | 38.5 | 34.7 | 40.9 |

2) *Multi-level optimization*: Fig. 4 shows the evolution of sampling patterns using our proposed multi-level optimization. Different widths of the B-spline kernels introduce different levels of improvement as the acquisition is optimized. Also shown are the results of multi-level optimization and a non-parametric trajectory as used in the first PILOT paper [29, version 1]. Directly optimizing sampling points seems only to introduce a small perturbation to the initialization.

3) *Effect of training set*: Fig. 5 shows radial-initialized trajectories trained by BJORK with brain and knee datasets. Different trajectories are learned from different datasets. We hypothesize that the difference is related to frequency distribution of energy, as well as the noise-level, which requires further study.

4) *Effect of reconstruction methods*: To test the influence of reconstruction methods on trajectory optimization, we tried a single image-domain refinement network as the reconstruction method in the joint learning model, similar to PILOT’s approach. Quadratic roughness penalty reconstruction in (8) still is the network’s input. The initialization of the sampling pattern is an undersampled radial trajectory. The proposed reconstruction method (unrolled neural network, UNN) improves reconstruction quality compared to a single end-to-end model, as shown in Table III. Such improvements are consistent with other comparisons between UNN methods and image-domain CNN methods using non-learned sampling patterns [34], [35], [37].

TABLE III

EFFECT OF DIFFERENT RECONSTRUCTION NETWORKS INVOLVED IN THE JOINT LEARNING MODEL

| | SSIM | PSNR(dB) |
|--------------|--------------|-------------|
| UNN | 0.968 | 37.0 |
| Single U-net | 0.933 | 32.7 |

5) *Phantom and in-vivo Experiments*: Fig. 6 shows water phantom results for different reconstruction algorithms. The rightmost column is the fully-sampled ground truth (Radial-full). Note that the unrolled neural network (UNN) here was trained with fastMRI brain dataset, and did not receive fine-tuning on the phantom dataset. The BJORK optimized trajectory leads to fewer artifacts and improved contrast for the UNN-based reconstruction.

Fig. 7 showcases one slice from the in-vivo experiment. For CS-based reconstruction, the undersampled radial trajectory exhibits stronger streak artifacts. The SPARKLING image has higher levels of ringing artifacts. CS reconstruction with the BJORK sampling pattern has less obvious artifacts but the tissue contrast is not as good as SPARKLING. For UNN-based reconstruction, all trajectories’ results show reductions of artifacts compared to CS-based reconstruction. The proposed method restores most of the structures and fine details, with minimal remaining artifacts. The contrast between grey and white matter seems suboptimal for all three methods. The reason may be that the acceleration ratio is too high ($20\times$) for recovering high-frequency details. Also, the short acquisition time (≈ 5 ms) and the GRE signal characteristics limit the SNR of the acquisition.

Supplementary Materials contain examples of reconstruction results before/after correction, and the measurement of actual trajectories.

V. DISCUSSION

This paper proposes an efficient learning-based framework for joint design of MRI sampling trajectories and reconstruction parameters. Defining an appropriate objective function for trajectory optimization is an open question. We circumvented this long-lasting problem by directly using the reconstruction quality as the training loss function in a supervised manner. The workflow includes a differentiable reconstruction algorithm for which the learning process obtains an intermediate gradient w.r.t. the reconstruction loss. However, solely depending on stochastic gradient descent cannot guarantee optimal results for this non-convex problem. To improve the training effect, we adopted several tricks, including trajectory parameterization, multi-level training, warm initialization of the reconstruction network, and an accurate approximation of NUFFT’s Jacobian. Results show that these approaches can stabilize the training and avoid sub-optimal local minima, or at least provide better local minima than previous methods.

We constructed an unrolled neural network-based reconstruction for non-Cartesian MRI data. In previous work, a single end-to-end network approach cannot efficiently remove aliasing artifacts. Additionally, the k-space “hard” data-consistency trick for data fidelity [50], [51] is inapplicable

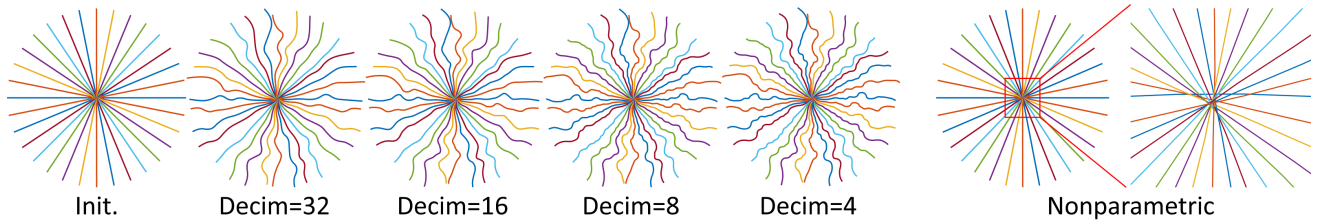


Fig. 4. The evolution of the learned trajectories. Decim means N_s/L in (3). Nonparametric means the locations of each sampling points are independent trainable variables, rather than being parameterized by quadratic B-spline kernels. The rightmost zoomed-in set shows the very small perturbations produced by the nonparametric approach.

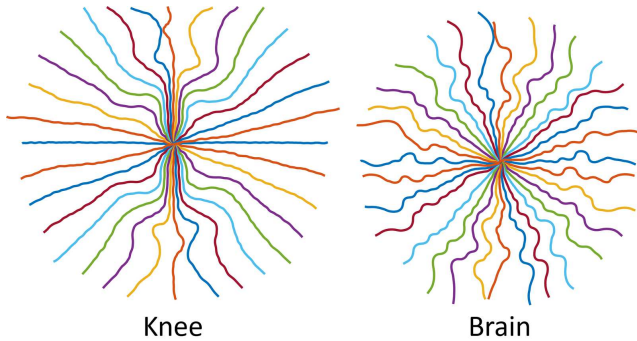


Fig. 5. Trajectories learned from different datasets.

for non-Cartesian sampling. An unrolled algorithm can reach a balance between data fidelity and the de-aliasing effect across multiple iterations. For 3D trajectory design using the proposed approach, the unrolled method’s memory consumption can be very large. More memory-efficient reconstruction models, such as the memory efficient network [52] can be explored in further study.

For learning-based medical imaging algorithms, one main obstacle towards clinical application is the gap between simulation and the physical world. Some factors include the following.

First, inconsistency exists between the training datasets and real-world acquisition, such as different vendors and protocols, posing a challenge to reconstruction algorithms’ robustness and generalizability. Our training dataset consisted of T1w/T2w/FLAIR Fast Spin-Echo (FSE or TSE) sequences, acquired on Siemens 1.5T/3.0T scanners. The number of receiver channels includes 4, 8, and 16, etc. We conducted the in-vivo/phantom experiment on a 3.0T GE scanner equipped with a 32-channel coil. The sequence is a T1w GRE sequence that has lower SNR compared to FSE sequences in the training set. Despite the very large differences with the training set, our work still demonstrated improved and robust results in the in-vivo and phantom experiment. We hypothesize that several factors could contribute to the results: (1) the reconstruction network uses the quadratic roughness penalized reconstruction as the initialization, normalized by the median value. Previous works typically use the adjoint reconstruction as the input of the network. In comparison, our regularized initialization helps provide consistency between different protocols, without too much compromise of the computation time/complexity,

(2) the PSF of the learned trajectory has a compact central-lobe, without large streak artifacts. Thus the reconstruction is basically a de-blurring/denoising task that is a local low-level problem and thus may require less training data than de-aliasing problems. For de-blurring of natural images, networks are usually adaptive to different noise levels and color spaces, and require small cohorts of data [53], [54]. In contrast, a CNN applied to an adjoint reconstruction must remove global aliasing artifacts, such as the streak and ringing artifacts for trajectories like radial and SPARKLING. The dynamics behind the neural network’s ability to resolve such artifacts is still an unsolved question, and the training may require a large amount of diverse data.

Secondly, it not easy to simulate system imperfections like eddy currents and off-resonance in the training phase. These imperfections can greatly affect image quality in practice. We used a trajectory measurement method to correct for the eddy-current effect. Future work will incorporate field inhomogeneity into the workflow.

Furthermore, even though the BJORK sampling was optimized for a UNN reconstruction method, the results in Fig. 6 and Fig. 7 suggest that the learned trajectory is also useful with a CS-based reconstruction method or other model-based reconstruction algorithms. This approach can still noticeably improve the image quality by simply replacing the readout waveform in the existing workflow, promoting the applicability of the proposed approach. We plan to apply the general framework to optimize a trajectory for (convex) CS-based reconstruction and compare to the (non-convex) open-loop UNN approach in future work.

Though the proposed trajectory is learned via a data-driven approach, it can also reflect the ideas behind SPARKLING and Poisson disk sampling: sampling patterns having large gaps or tight clusters of points are inefficient, and the sampling points should be somewhat evenly distributed (but not too uniform). Furthermore, our method appeared to have learned some latent characteristics, like the conjugate symmetry for these spin-echo training datasets. To combine both methods’ strength, a promising future direction is to use SPARKLING as a primed initialization of BJORK.

The network is trained on a big public data set. In the experiment, knee imaging and brain imaging led to different learned trajectories. This demonstrates that the data set can greatly influence the optimization results. We also implemented a complementary experiment on a smaller training set (results not shown). We found that a small subset (3000 slices) also

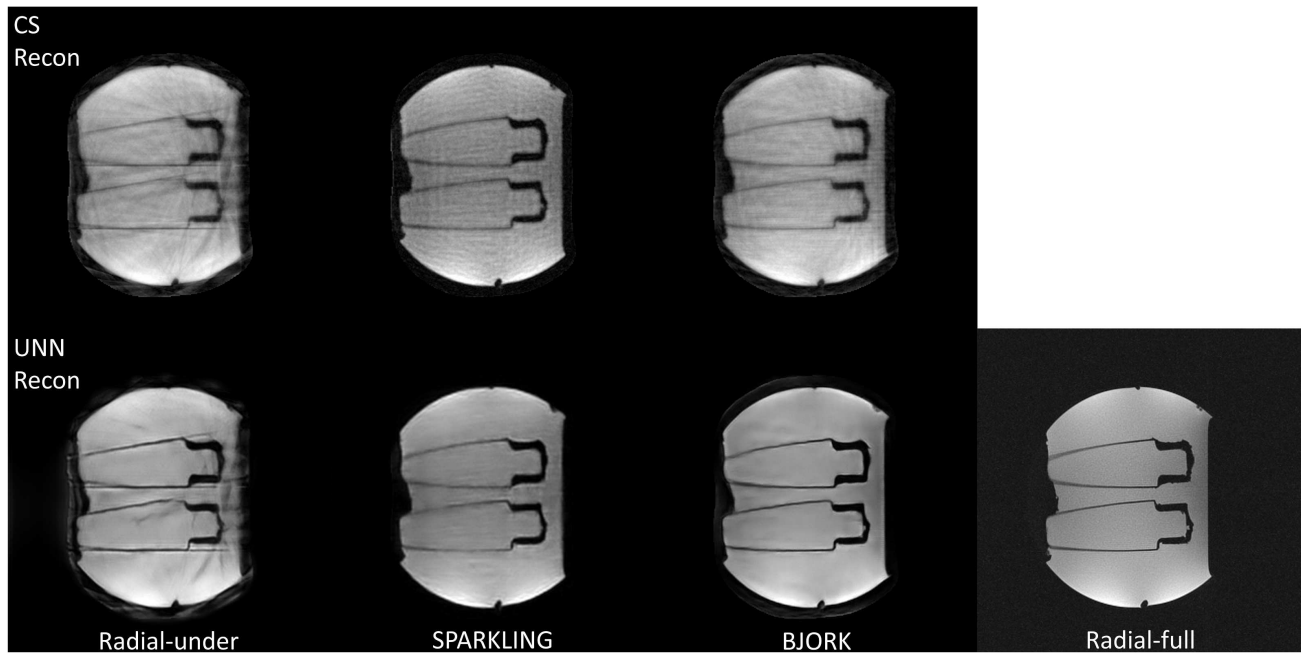


Fig. 6. Representative results of the phantom experiment using CS-based and UNN-based reconstruction algorithms. The sequences involved were radial-like GRE (detailed in Table I). The readout length was 2.56 ms, and we used 16/320 spokes for undersampled (Radial-Under, SPARKLING, BJORK) trajectories and the fully-sampled radial trajectory.

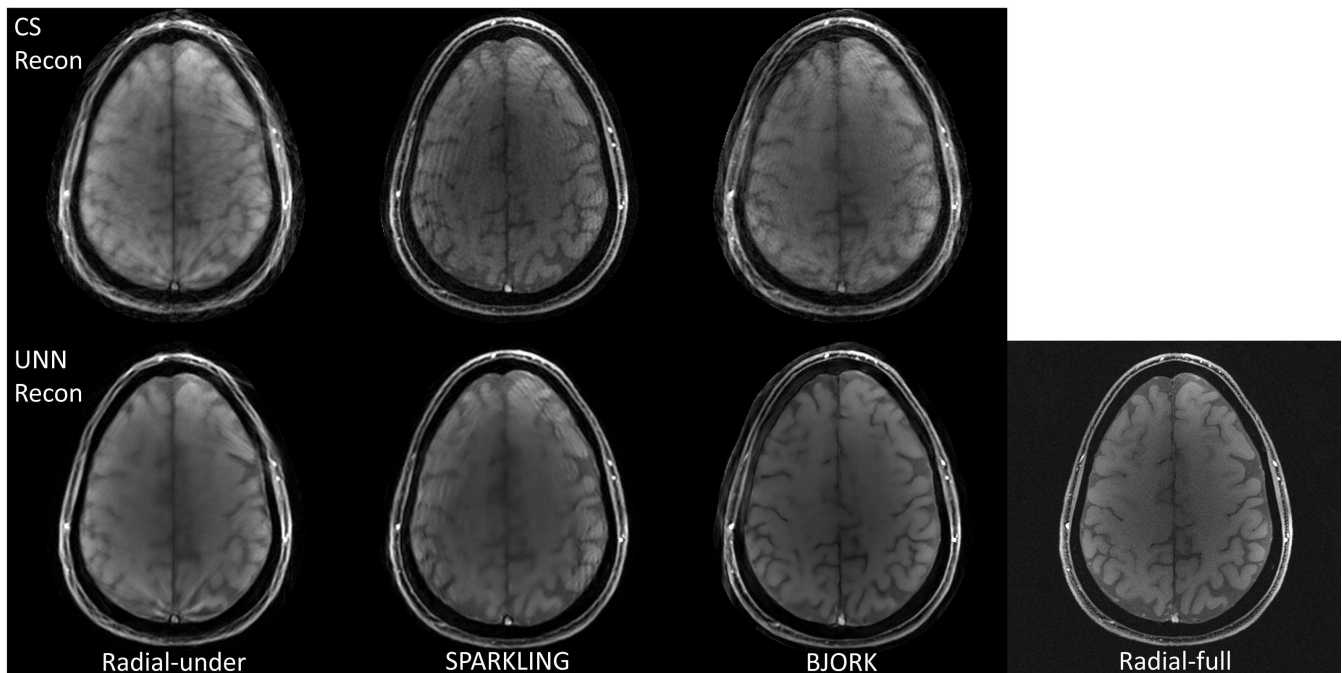


Fig. 7. Results of the in-vivo experiment. The trajectories were also radial-like (detailed in Table I). The readout time was 5.12 ms. The number of shots for undersampled trajectories was 16, and for the fully-sampled radial trajectory is 320 (20 \times acceleration). The FOV was 22cm.

led to similar learned trajectories. Therefore, for some organs where a sizeable dataset is not publicly available, this approach may still work with small-scale private datasets. To examine the influence of scanner models, field strength, and sequences, following studies should investigate more diversity in datasets.

The eddy-current effect poses a long-term problem for non-Cartesian trajectories and impedes their widespread clinical usage. This work used a simple k-space mapping technique as the correction method. The downside of this method is its long calibration time, although it can be performed in the scanner's idle time. This method is waveform-specific, which means that correction should be done for different trajectories. Other methods relying on field probes can get a more accurate correction with less time. However, this approach demands dedicated hardware. In a future study, the eddy current-related artifacts could be simulated according to the GIRF model in the training phase, so that the trajectory is learned to be robust against the eddy current effect.

Aside from practical challenges with GPU memory, the general approach described here is readily extended from 2D to 3D sampling trajectories. A more challenging future direction is to extend the work to dynamic imaging applications like fMRI and cardiac imaging, where both the sampling pattern and the reconstruction method should exploit redundancies in the time dimension, e.g., using low-rank models [55].

ACKNOWLEDGMENT

The authors thank Dr. Melissa Haskell and Naveen Murthy from University of Michigan for helpful advice and fruitful discussions.

REFERENCES

- [1] P. C. Lauterbur, "Image formation by induced local interactions: examples employing nuclear magnetic resonance," *Nature*, vol. 242, no. 5394, pp. 190–191, 1973.
- [2] C. B. Ahn, J. H. Kim, and Z. H. Cho, "High-speed spiral-scan echo planar NMR imaging-I," *IEEE Trans. Med. Imag.*, vol. 5, no. 1, pp. 2–7, Mar. 1986.
- [3] D. J. Larkman and R. G. Nunes, "Parallel magnetic resonance imaging," *Phys. Med. Biol.*, vol. 52, no. 7, pp. R15–R55, Mar. 2007.
- [4] Z. Wang and G. R. Arce, "Variable density compressed image sampling," *IEEE Trans. Image Proc.*, vol. 19, no. 1, pp. 264–270, Jan. 2010.
- [5] F. Knoll, C. Clason, C. Diwoky, and R. Stollberger, "Adapted random sampling patterns for accelerated MRI," *Magn. Reson. Mater. Phys. Biol. Med.*, vol. 24, no. 1, pp. 43–50, Feb. 2011.
- [6] M. Seeger, H. Nickisch, R. Pohmann, and B. Schölkopf, "Optimization of k-space trajectories for compressed sensing by Bayesian experimental design," *Magn. Reson. Med.*, vol. 63, no. 1, pp. 116–126, 2010.
- [7] N. Chauffert, P. Ciuciu, and P. Weiss, "Variable density compressed sensing in MRI. Theoretical vs heuristic sampling strategies," in *2013 IEEE 10th Intl. Symp. on Biomed. Imag. (ISBI)*, Apr. 2013, pp. 298–301.
- [8] R. K. Robison, Z. Li, D. Wang, M. B. Ooi, and J. G. Pipe, "Correction of B0 eddy current effects in spiral MRI," *Magn. Reson. Med.*, vol. 81, no. 4, pp. 2501–2513, 2019.
- [9] J. H. Lee, B. A. Hargreaves, B. S. Hu, and D. G. Nishimura, "Fast 3D imaging using variable-density spiral trajectories with applications to limb perfusion," *Magn. Reson. Med.*, vol. 50, no. 6, pp. 1276–1285, 2003.
- [10] S. Winkelman, T. Schaeffter, T. Koehler, H. Eggers, and O. Doessel, "An optimal radial profile order based on the golden ratio for time-resolved MRI," *IEEE Trans. Med. Imag.*, vol. 26, no. 1, pp. 68–76, Jan. 2007.
- [11] B. Bilgic *et al.*, "Wave-CAIPI for highly accelerated 3D imaging," *Magn. Reson. Med.*, vol. 73, no. 6, pp. 2152–2162, 2015.
- [12] A. Bilgin, T. Troouard, A. Gmitro, and M. Altbach, "Randomly perturbed radial trajectories for compressed sensing MRI," in *Proc. Intl. Soc. Magn. Reson. Med. (ISMRM)*, vol. 16, 2008, p. 3152.
- [13] M. Lustig, S. Kim, and J. M. Pauly, "A fast method for designing time-optimal gradient waveforms for arbitrary k-space trajectories," *IEEE Trans. Med. Imag.*, vol. 27, no. 6, pp. 866–873, Jun. 2008.
- [14] S. Sabat, R. Mir, M. Guarini, A. Guesalaga, and P. Irarrazaval, "Three dimensional k-space trajectory design using genetic algorithms," *Magn. Reson. Imag.*, vol. 21, no. 7, pp. 755–764, Sep. 2003.
- [15] C. Lazarus *et al.*, "SPARKLING: variable-density k-space filling curves for accelerated T2*-weighted MRI," *Mag. Res. Med.*, vol. 81, no. 6, pp. 3643–61, Jun. 2019.
- [16] W. Fong and E. Darve, "The black-box fast multipole method," *J. Comput. Phys.*, vol. 228, no. 23, pp. 8712–8725, Dec. 2009.
- [17] N. Chauffert, P. Weiss, J. Kahn, and P. Ciuciu, "A projection algorithm for gradient waveforms design in magnetic resonance imaging," *IEEE Trans. Med. Imag.*, vol. 35, no. 9, pp. 2026–2039, Sep. 2016.
- [18] S. Elmalem, R. Giryes, and E. Marom, "Learned phase coded aperture for the benefit of depth of field extension," *Opt. Exp.*, vol. 26, no. 12, pp. 15 316–15 331, Jun. 2018.
- [19] I. A. M. Huijben, B. S. Veeling, K. Janse, M. Mischi, and R. J. G. van Sloun, "Learning sub-sampling and signal recovery with applications in ultrasound imaging," *IEEE Trans. Med. Imag.*, vol. 39, no. 12, pp. 3955–3966, Dec. 2020.
- [20] C. D. Bahadir, A. Q. Wang, A. V. Dalca, and M. R. Sabuncu, "Deep-learning-based optimization of the under-sampling pattern in MRI," *IEEE Trans. Comput. Imag.*, vol. 6, pp. 1139–1152, 2020.
- [21] I. A. M. Huijben, B. S. Veeling, and R. J. G. van Sloun, "Learning sampling and model-based signal recovery for compressed sensing MRI," in *2020 IEEE Intl. Conf. on Acous., Speech and Sig. Proc. (ICASSP)*, May 2020, pp. 8906–8910.
- [22] T. Sanchez *et al.*, "Scalable learning-based sampling optimization for compressive dynamic MRI," in *2020 IEEE Intl. Conf. on Acous., Speech and Sig. Proc. (ICASSP)*, May 2020, pp. 8584–8588.
- [23] M. V. Zibetti, G. T. Herman, and R. R. Regatte, "Fast data-driven learning of MRI sampling pattern for large scale problems," 2020. [Online]. Available: <http://arxiv.org/abs/2011.02322>
- [24] C. Qian, Y. Yu, and Z.-H. Zhou, "Subset selection by Pareto optimization," in *Proc. Intl. Conf. Neur. Info. Proc. Sys. (NeurIPS)*, ser. NIPS'15, Dec. 2015, pp. 1774–1782.
- [25] K. H. Jin, M. Unser, and K. M. Yi, "Self-supervised deep active accelerated MRI," 2020. [Online]. Available: <http://arxiv.org/abs/1901.04547>
- [26] D. Zeng, C. Sandino, D. Nishimura, S. Vasanawala, and J. Cheng, "Reinforcement learning for online undersampling pattern optimization," in *Proc. Intl. Soc. Magn. Reson. Med. (ISMRM)*, 2019, p. 1092.
- [27] F. Sherry *et al.*, "Learning the sampling pattern for MRI," 2020. [Online]. Available: <http://arxiv.org/abs/1906.08754>
- [28] H. K. Aggarwal and M. Jacob, "Joint optimization of sampling patterns and deep priors for improved parallel MRI," in *2020 IEEE Intl. Conf. on Acous., Speech and Sig. Proc. (ICASSP)*, May 2020, pp. 8901–8905.
- [29] T. Weiss, O. Senouf, S. Vedula, O. Michailovich, M. Zibulevsky, and A. Bronstein, "PILOT: physics-informed learned optimal trajectories for accelerated MRI," 2019. [Online]. Available: <http://arxiv.org/abs/1909.05773>
- [30] O. Ronneberger, P. Fischer, and T. Brox, "U-Net: convolutional networks for biomedical image segmentation," in *Med. Imag. Comput. and Comput.-Assist. Interv. (MICCAI)*, 2015, pp. 234–241.
- [31] K. P. Pruessmann, M. Weiger, P. Börnert, and P. Boesiger, "Advances in sensitivity encoding with arbitrary k-space trajectories," *Magn. Reson. Med.*, vol. 46, no. 4, pp. 638–651, 2001.
- [32] S. Hao, J. A. Fessler, D. C. Noll, and J.-F. Nielsen, "Joint design of excitation k-space trajectory and RF pulse for small-tip 3D tailored excitation in MRI," *IEEE Trans. Med. Imag.*, vol. 35, no. 2, pp. 468–479, Feb. 2016.
- [33] F. J. Nielsen JF, Sun H and N. DC, "Improved gradient waveforms for small-tip 3D spatially tailored excitation using iterated local search," in *Proc. Intl. Soc. Magn. Reson. Med. (ISMRM)*, 2016, p. 1013.
- [34] H. K. Aggarwal, M. P. Mani, and M. Jacob, "MoDL: model-based deep learning architecture for inverse problems," *IEEE Trans. Med. Imag.*, vol. 38, no. 2, pp. 394–405, Feb. 2019.
- [35] Y. Yang, J. Sun, H. Li, and Z. Xu, "Deep ADMM-Net for compressive sensing MRI," in *Proc. of the 30th Intl. Conf. on Neur. Info. Proc. Sys. (NIPS)*, Dec. 2016, pp. 10–18.
- [36] K. Hammernik *et al.*, "Learning a variational network for reconstruction of accelerated MRI data," *Magn. Reson. Med.*, vol. 79, no. 6, pp. 3055–3071, 2018.

- [37] J. Schlemper, C. Qin, J. Duan, R. M. Summers, and K. Hammernik, "Sigma-net: ensembled iterative deep neural networks for accelerated parallel MR image reconstruction," 2020. [Online]. Available: <http://arxiv.org/abs/1912.05480>
- [38] J. A. Fessler, S. Lee, V. T. Olafsson, H. R. Shi, and D. C. Noll, "Toeplitz-based iterative image reconstruction for MRI with correction for magnetic field inhomogeneity," *IEEE Trans. Sig. Proc.*, vol. 53, no. 9, pp. 3393–402, Sep. 2005.
- [39] K. Gregor and Y. LeCun, "Learning fast approximations of sparse coding," in *Proc. of the 27th Intl. Conf. on Mach. Learn. (ICML)*, Jun. 2010, pp. 399–406.
- [40] S. Yu, B. Park, and J. Jeong, "Deep iterative down-up CNN for image denoising," in *Proc. of the IEEE Conf. on Comput. Vis. and Patt. Recog. Work. (CVPRW)*, 2019, pp. 0–0.
- [41] S. J. Vannesjo *et al.*, "Gradient system characterization by impulse response measurements with a dynamic field camera," *Magn. Reson. Med.*, vol. 69, no. 2, pp. 583–593, 2013.
- [42] J. H. Duyn, Y. Yang, J. A. Frank, and J. W. van der Veen, "Simple correction method for k-space trajectory deviations in MRI," *J. Magn. Reson.*, vol. 132, pp. 150–153, May 1998.
- [43] J.-F. Nielsen and D. C. Noll, "TOPPE: a framework for rapid prototyping of MR pulse sequences," *Magn. Reson. Med.*, vol. 79, no. 6, pp. 3128–3134, 2018.
- [44] C. Lazarus, "Compressed sensing in MRI: optimization-based design of k-space filling curves for accelerated MRI," Ph.D. dissertation, Université Paris Saclay (COMUE), Sep. 2018.
- [45] A. Horé and D. Ziou, "Image quality metrics: PSNR vs. SSIM," in *Intl. Conf. on Patn. Recog. (ICPR)*, Aug. 2010, pp. 2366–2369.
- [46] J. H. Lee, B. A. Hargreaves, B. S. Hu, and D. G. Nishimura, "Fast 3D imaging using variable-density spiral trajectories with applications to limb perfusion," *Magn. Reson. Med.*, vol. 50, no. 6, pp. 1276–1285, 2003.
- [47] J. Zbontar *et al.*, "fastMRI: An open dataset and benchmarks for accelerated MRI," 2018. [Online]. Available: <http://arxiv.org/abs/1811.08839>
- [48] M. Uecker *et al.*, "ESPIRiT - an eigenvalue approach to autocalibrating parallel MRI: where SENSE meets GRAPPA," *Mag. Reson. Med.*, vol. 71, no. 3, pp. 990–1001, Mar. 2014.
- [49] D. P. Kingma and J. Ba, "Adam: a method for stochastic optimization," 2017. [Online]. Available: <http://arxiv.org/abs/1412.6980>
- [50] M. Mardani *et al.*, "Deep generative adversarial neural networks for compressive sensing MRI," *IEEE Trans. Med. Imag.*, vol. 38, no. 1, pp. 167–179, 2018.
- [51] J. Schlemper, J. Caballero, J. V. Hajnal, A. N. Price, and D. Rueckert, "A deep cascade of convolutional neural networks for dynamic MR image reconstruction," *IEEE Trans. Med. Imag.*, vol. 37, no. 2, pp. 491–503, Feb. 2018.
- [52] S. C. van de Leemput, J. Teuwen, B. van Ginneken, and R. Manniesing, "MemCNN: a Python/PyTorch package for creating memory-efficient invertible neural networks," *J. Open Source Softw.*, vol. 4, no. 39, p. 1576, Jul. 2019.
- [53] S. Nah *et al.*, "NTIRE 2020 challenge on image and video deblurring," in *Proc. of the IEEE Conf. on Comput. Vis. and Patt. Recog. Work. (CVPRW)*, 2020, pp. 416–417.
- [54] A. Lugmayr *et al.*, "NTIRE 2020 challenge on real-world image super-resolution: methods and results," in *Proc. of the IEEE Conf. on Comput. Vis. and Patt. Recog. Work. (CVPRW)*, 2020, pp. 494–495.
- [55] M. Jacob, M. P. Mani, and J. C. Ye, "Structured low-rank algorithms: theory, MR applications, and links to machine learning," *IEEE Sig. Proc. Mag.*, vol. 37, no. 1, pp. 54–68, Jan. 2020.
- [56] J. A. Fessler, "Model-based image reconstruction for MRI," *IEEE Sig. Proc. Mag.*, vol. 27, no. 4, pp. 81–89, 2010.
- [57] J. A. Fessler and B. P. Sutton, "Nonuniform fast Fourier transforms using min-max interpolation," *IEEE Trans. Sig. Proc.*, vol. 51, no. 2, pp. 560–74, Feb. 2003.
- [58] B. Dale, M. Wendt, and J. L. Duerk, "A rapid look-up table method for reconstructing MR images from arbitrary k-space trajectories," *IEEE Trans. Med. Imag.*, vol. 20, no. 3, pp. 207–217, 2001.
- [59] M. J. Muckley, R. Stern, T. Murrell, and F. Knoll, "TorchKbNufft: A high-level, hardware-agnostic non-uniform fast fourier transform," in *ISMRM Workshop on Data Sampling & Image Reconstruction*, 2020.

APPENDIX

A. Experiments

1) *Eddy-current effect*: Fig. S1 displays the CS-based reconstruction of real acquisitions according to nominal/measured trajectories. Fig. S2 shows the measurement results of the trajectories. Using the measurement of the actual trajectory seems to mitigate the influence of eddy current effects in the reconstruction results.

2) *Simulation Experiments*: Fig. S3 shows examples of the UNN-based reconstruction for different trajectories in the simulation experiment. Compared with undersampled radial trajectory or SPARKLING trajectory, the proposed BJORK trajectory leads to a lower level of artifacts and better restoration of fine structures.

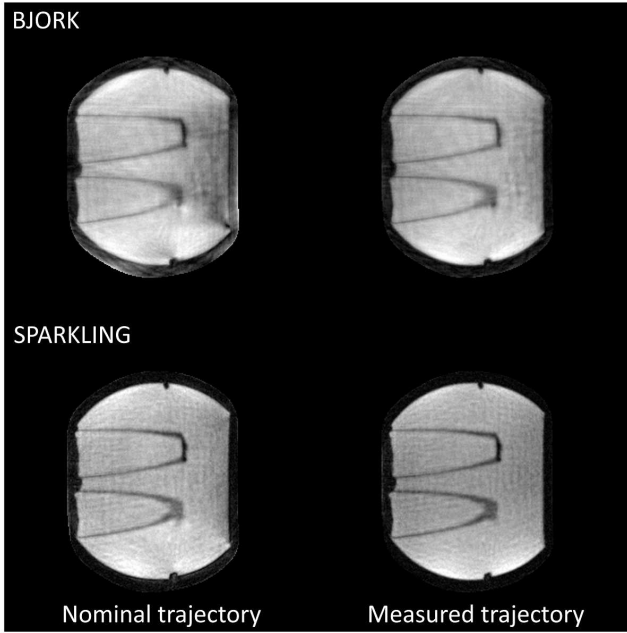


Fig. S1. CS-based reconstruction of a water phantom. The left column is the reconstruction with the nominal trajectory, and right is with the measured trajectory. Reconstruction with the mapped trajectory introduces fewer artifacts.

B. Efficient backpropagation of NUFFT operators

This section describes an efficient approximation for the Jacobian of the NUFFT operation used in the MRI system model for non-Cartesian sampling. This approximation facilitates fast and accurate backpropagation methods for learning non-Cartesian k-space trajectories.

Consider the (single-coil) MRI measurement model [56]

$$\mathbf{y} = \mathbf{A}\mathbf{x} + \boldsymbol{\varepsilon}$$

$\mathbf{y} \in \mathbb{C}^M$, $\mathbf{x} \in \mathbb{C}^N$, $\mathbf{A} \in \mathbb{C}^{M \times N}$ where $\mathbf{A} = \mathbf{A}(\boldsymbol{\omega})$ has elements

$$a_{ij} = e^{-i\vec{\omega}_i \cdot \vec{r}_j}$$

for $\vec{\omega}_i \in \mathbb{R}^D$ and $\vec{r}_j \in \mathbb{R}^D$ where $D \in \{1, 2, 3\}$ denotes the image dimension, and where

$$\boldsymbol{\omega} = [\boldsymbol{\omega}^{[1]} \ \boldsymbol{\omega}^{[2]} \ \dots \ \boldsymbol{\omega}^{[D]}]$$

is the $M \times d$ vector representation of all the k-space sampling locations and $\boldsymbol{\omega}^{[d]} \in \mathbb{R}^M$ denotes its d th column. N denotes the number of voxels, and M stands for the number of acquisition (in k-space). Typically \mathbf{A} is approximated by a NUFFT operator [57].

For simplicity, consider the training loss of trajectory optimization for a single image (or a mini-batch):

$$L(\boldsymbol{\omega}) = \|f_{\boldsymbol{\theta}, \boldsymbol{\omega}}(\boldsymbol{\omega}; \mathbf{A}(\boldsymbol{\omega})\mathbf{x} + \boldsymbol{\varepsilon}) - \mathbf{x}\|,$$

where $\mathbf{x} \in \mathbb{C}^N$. Note that $L: \mathbb{R}^M \mapsto \mathbb{R}$ so $\nabla L \in \mathbb{R}^M$.

The update w.r.t. $L(\boldsymbol{\omega})$ involves the gradients w.r.t. NUFFT operators $\mathbf{A}(\boldsymbol{\omega})$ and its adjoint. Previous works [29] propagate the gradient calculations through all of the NUFFT steps using the chain rule, which is potentially slow, and could introduce error because of the interpolation operators. Here we investigate a different approach where we analyze on paper the gradient using the exact (slow) Fourier transform expression and then implement that expression using (fast) NUFFT approximations. This approach leads to inexact gradient computations, but gradients are often inexact in machine learning problems anyway, due to operations like mini-batches.

1) *Forward operator*: For \mathbf{x} :

$$\frac{\partial \mathbf{A}\mathbf{x}}{\partial \mathbf{x}} = \mathbf{A}.$$

For the d th column of $\boldsymbol{\omega}$:

$$\begin{aligned} \left[\frac{\partial \mathbf{A}\mathbf{x}}{\partial \boldsymbol{\omega}^{[d]}} \right]_{il} &= \frac{\partial [\mathbf{A}\mathbf{x}]_i}{\partial \omega_l^{[d]}} \\ &= \frac{\partial}{\partial \omega_l^{[d]}} \sum_{j=1}^N e^{-i\vec{\omega}_i \cdot \vec{r}_j} x_j \\ &= \begin{cases} -i \sum_{j=1}^N e^{-i\vec{\omega}_i \cdot \vec{r}_j} x_j r_j^{[d]}, & i = l \\ 0, & \text{otherwise,} \end{cases} \end{aligned}$$

for $i, l = 1, \dots, M$. By denoting the point-wise vector product as \odot , the above summation equals the product of the i th row of \mathbf{A} with $\mathbf{x} \odot \mathbf{r}^{[d]}$. Thus the $M \times M$ Jacobian matrix for the partial derivatives of $\mathbf{A}\mathbf{x}$ w.r.t. $\boldsymbol{\omega}^{[d]}$ is:

$$\frac{\partial \mathbf{A}\mathbf{x}}{\partial \boldsymbol{\omega}^{[d]}} = -i \text{diag} \left\{ \mathbf{A}(\mathbf{x} \odot \mathbf{r}^{[d]}) \right\}. \quad (\text{S.1})$$

Thus, to apply this Jacobian to a (gradient) vector $\mathbf{v} \in \mathbb{C}^M$, as needed in a back-propagation step, we simply compute

$$-i (\mathbf{A}(\mathbf{x} \odot \mathbf{r}^{[d]})) \odot \mathbf{v},$$

by applying a NUFFT operation \mathbf{A} to $\mathbf{x} \odot \mathbf{r}^{[d]}$.

2) *Adjoint operator*: For \mathbf{y} :

$$\frac{\partial \mathbf{A}'\mathbf{y}}{\partial \mathbf{y}} = \mathbf{A}'$$

For the d th column of $\boldsymbol{\omega}$, the $N \times M$ Jacobian matrix has elements:

$$\begin{aligned} \left[\frac{\partial \mathbf{A}'\mathbf{y}}{\partial \boldsymbol{\omega}^{[d]}} \right]_{jl} &= \frac{\partial [\mathbf{A}'\mathbf{y}]_j}{\partial \omega_l^{[d]}} \\ &= \frac{\partial \sum_{i=1}^M e^{i\vec{\omega}_i \cdot \vec{r}_j} y_i}{\partial \omega_l^{[d]}} \\ &= i e^{i\vec{\omega}_l \cdot \vec{r}_j} y_l r_j^{[d]}. \end{aligned}$$

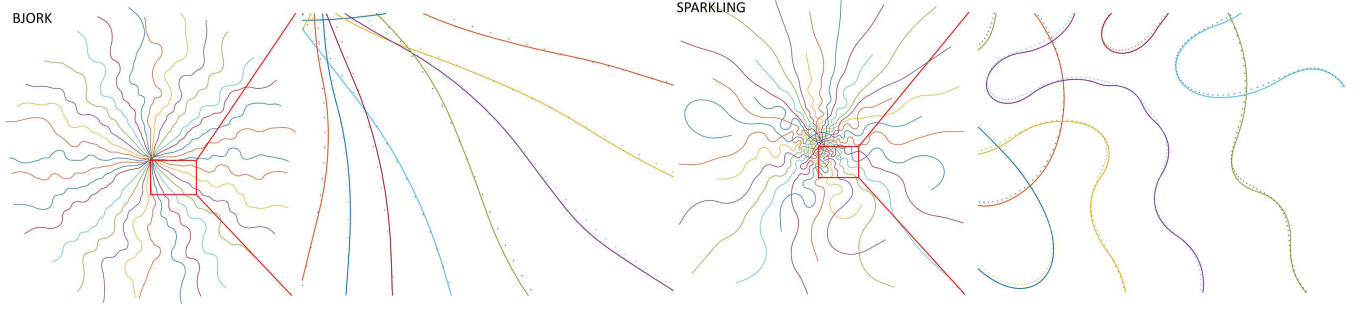


Fig. S2. The measurement of the influence of the eddy currents on readout waveform. The solid line is the nominal trajectory, and the dotted line is the measurement.

Thus the Jacobian matrix is

$$\frac{\partial \mathbf{A}' \mathbf{y}}{\partial \boldsymbol{\omega}^{[d]}} = \imath \text{diag}\{\mathbf{r}^{[d]}\} \mathbf{A}' \text{diag}\{\mathbf{y}\}. \quad (\text{S.2})$$

Applying this Jacobian to a vector $\mathbf{v} \in \mathbb{C}^M$ involves an adjoint NUFFT \mathbf{A}' of $\mathbf{y} \odot \mathbf{v}$.

3) *Frame operator (Gram matrix)*: For \mathbf{x} :

$$\frac{\partial \mathbf{A}' \mathbf{A} \mathbf{x}}{\partial \mathbf{x}} = \mathbf{A}' \mathbf{A}.$$

For the d th column of $\boldsymbol{\omega}$, the elements of the $N \times M$ Jacobian matrix are

$$\begin{aligned} \left[\frac{\partial \mathbf{A}' \mathbf{A} \mathbf{x}}{\partial \boldsymbol{\omega}^{[d]}} \right]_{kl} &= \frac{\partial [\mathbf{A}' \mathbf{A} \mathbf{x}]_k}{\partial \omega_l^{[d]}} \\ &= \frac{\partial \sum_{i=1}^M \sum_{j=1}^N e^{-\imath \bar{\omega}_l \cdot (\bar{r}_j - \bar{r}_k)} x_j}{\partial \omega_l^{[d]}} \\ &= -\imath \sum_{j=1}^N e^{-\imath \bar{\omega}_l \cdot (\bar{r}_j - \bar{r}_k)} x_j (r_j^{[d]} - r_k^{[d]}) \\ &= -\imath e^{\imath \bar{\omega}_l \cdot \bar{r}_k} \sum_{j=1}^N e^{-\imath \bar{\omega}_l \cdot \bar{r}_j} x_j r_j^{[d]} \\ &\quad + \imath e^{\imath \bar{\omega}_l \cdot \bar{r}_k} r_k^{[d]} \sum_{j=1}^N e^{-\imath \bar{\omega}_l \cdot \bar{r}_j} x_j. \end{aligned}$$

Thus the Jacobian matrix is:

$$\begin{aligned} \frac{\partial \mathbf{A}' \mathbf{A} \mathbf{x}}{\partial \boldsymbol{\omega}^{[d]}} &= -\imath \mathbf{A}' \text{diag}\{\mathbf{A}(\mathbf{x} \odot \mathbf{r}^{[d]})\} \\ &\quad + \imath \text{diag}\{\mathbf{r}^{[d]}\} \mathbf{A}' \text{diag}\{\mathbf{A} \mathbf{x}\}. \quad (\text{S.3}) \end{aligned}$$

Again, we apply this Jacobian to a vector by combining NUFFT operations with Hadamard products.

TABLE S.1
COMPUTATION TIME

| | auto-diff | approx. |
|--|-----------|---------|
| Large image - GPU | 1.31s | 0.91s |
| Small image - GPU | 1.29s | 0.90s |
| Large image - CPU | 4.32s | 0.74s |
| Small image - CPU | 0.71s | 0.36s |
| Large size: 320*320; small size: 40*40 | | |

4) *Validation*: For validation, we examined a simple test case with different calculation methods. We computed

$$\frac{\partial \|\mathbf{A}' \mathbf{A} \mathbf{x}\|_2^2}{\partial \boldsymbol{\omega}^{[d]}} \quad \text{and} \quad \frac{\partial \|\mathbf{A}' \mathbf{A} \mathbf{x}\|_2^2}{\partial \mathbf{x}},$$

where \mathbf{x} is a cropped Shepp–Logan phantom with random additional phase in $[-\pi, \pi]$. The sampling pattern is undersampled radial spokes. The \mathbf{x} and $\boldsymbol{\omega}$ displayed are one fragment of the whole vector. Three settings are compared: (1) auto-differentiation of NUFFT; the table finding operation [58] is replaced by bi-linear interpolation to enable auto-differentiation, (2) auto-differentiation of exact non-uniform discrete Fourier transform (NDFT), (3) our approximation. It is worth noting that there is no 'ground truth' here. Errors occur in the interpolation of (1). (2) is the accurate gradient of NDFT because the gradient calculation only involves one exponential and one sum operation, with no accumulation error. Since NUFFT is only an approximation of NDFT, we cannot directly regard NDFT's Jacobian as NUFFT's Jacobian. If the NUFFT operation is accurate enough, though, (2) can be a good approximation of NUFFT's Jacobian matrix. As a validation method, we also compared the trajectory optimization result by (1) and (3) (approach (2) is too time-consuming for this task.). The implementation of (1) and (3) were based on [59]. We jointly trained the reconstruction network and the trajectory as described in the main text, but did not parameterize the trajectory.

Fig. S4 and Fig. S5 show the gradient calculated by different methods. For gradients w.r.t. the image \mathbf{x} , three methods lead to similar results. For gradient concerning the trajectory $\boldsymbol{\omega}$, the auto-differentiation has larger deviance from the results of exact NDFT. If random phase is not added to the complex-valued image \mathbf{x} , the three methods still have similar results. So here we display an extreme case. In Fig. S6, our approximation method leads to a learned trajectory consistent with intuition: sampling points should not be clustered or too distant from each other. The quantitative reconstruction results also demonstrate significant improvement (950 test slices, SSIM: 0.930 vs. 0.957.).

Table S.1 compares the time for computing (1) and (2). The CPUs used are Intel Xeon Gold 6138 CPU @ 2.00GHz and GPU is an Nvidia RTX2080Ti. Our method is faster than auto-differentiation, especially in the CPU mode.

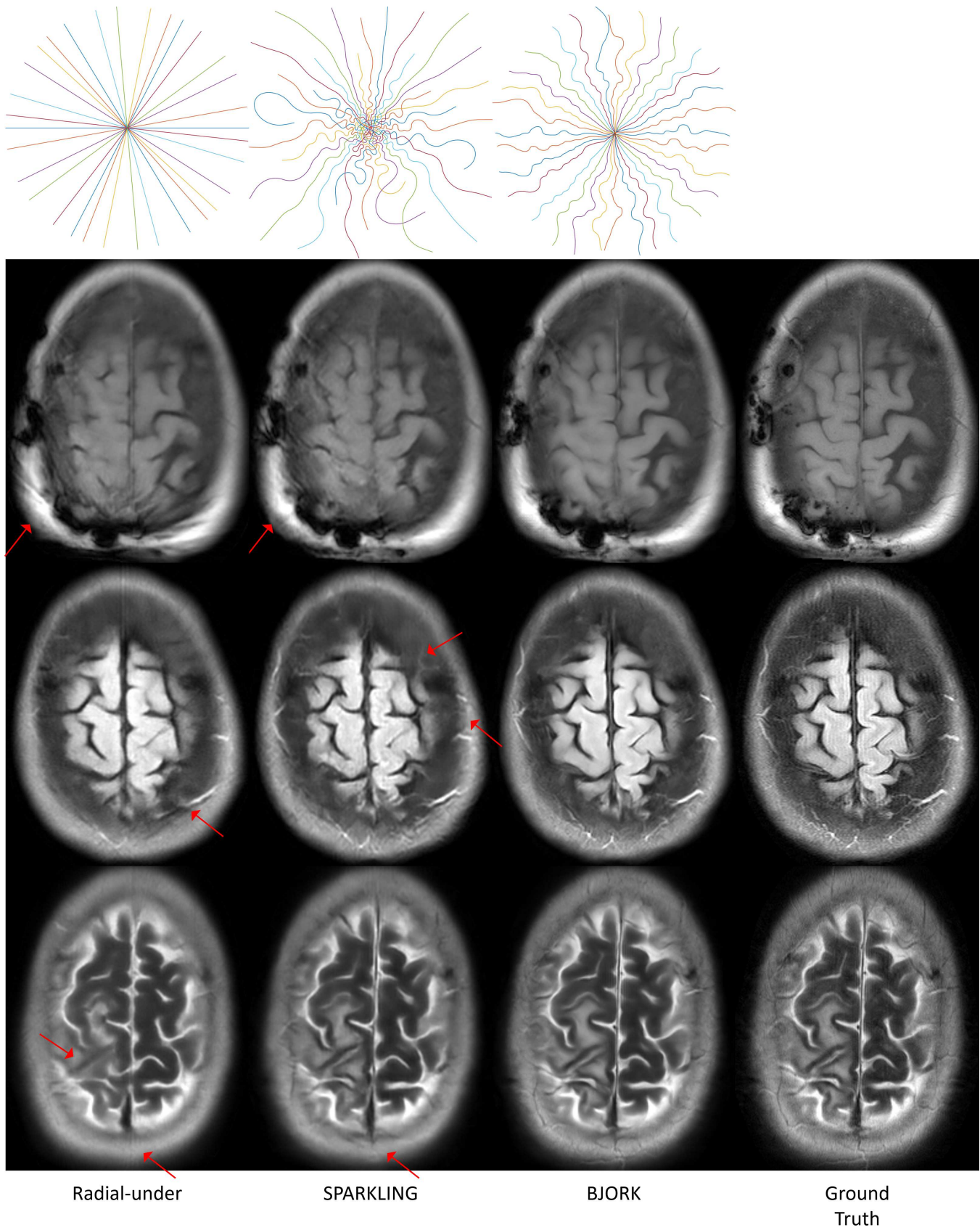


Fig. S3. Results from the simulation experiment using the UNN-based reconstruction algorithm for three different trajectories. The first row shows the trajectories.

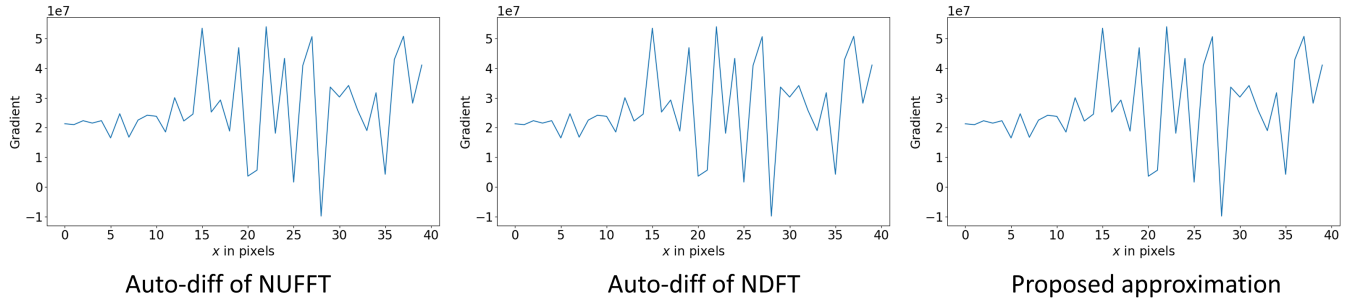


Fig. S4. The gradient w.r.t. image x . Three calculation methods lead to similar results.

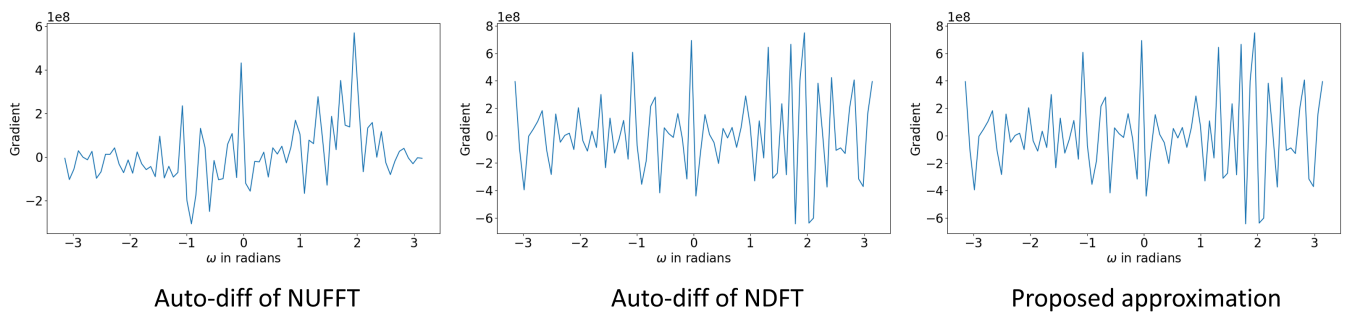


Fig. S5. The gradient w.r.t. trajectory ω . The proposed approximation better matches the gradient of the NDFT.

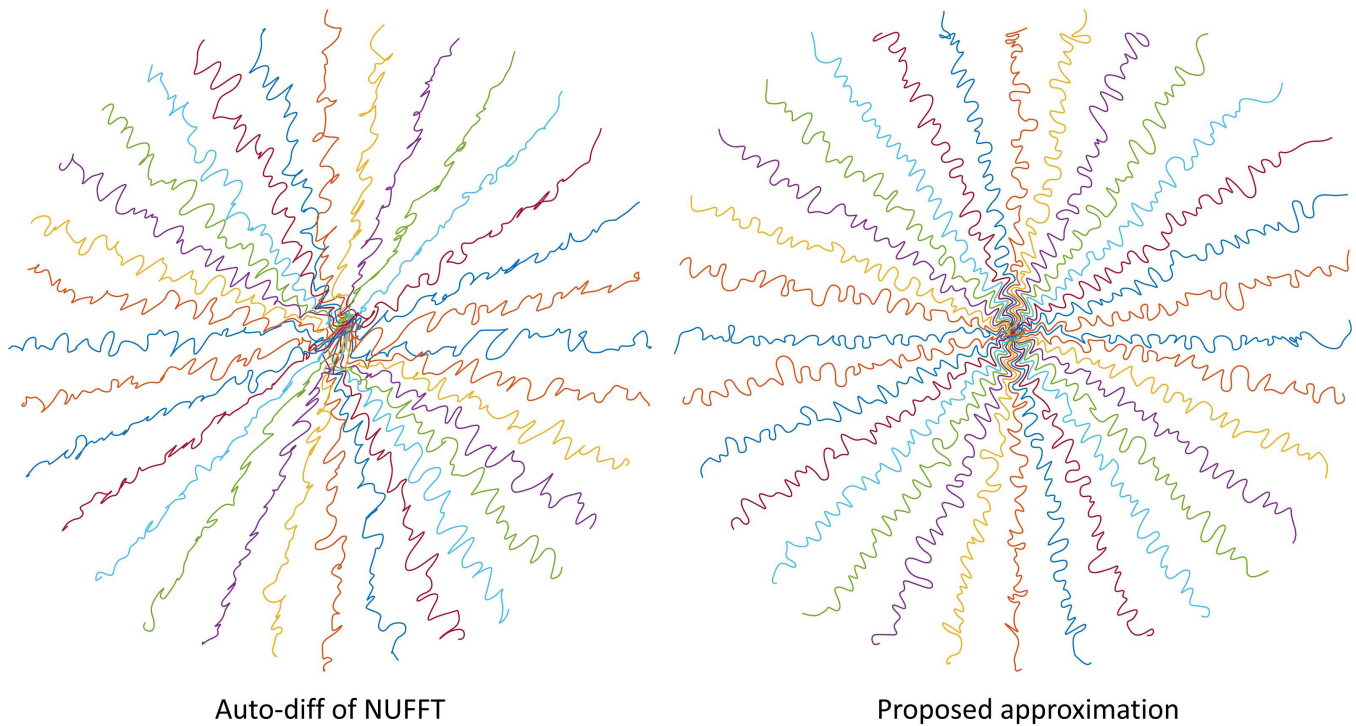


Fig. S6. The learned trajectories with descent directions calculated by different methods.